Materials and Interfaces

Article

Breath-Based SERS Detection of Propofol Metabolites during Anesthesia Using Mesoporous Au Foam Chips

Hui Zhang [1], Guanghui An [2], and Enduo Feng [1,*]

[1] Shanghai Key Laboratory of Anesthesiology and Brain Functional Modulation, Clinical Research Center for Anesthesiology and Perioperative Medicine, Translational Research Institute of Brain and Brain-Like Intelligence, Shanghai Fourth People's Hospital, School of Medicine, Tongji University, Shanghai 200434, China
[2] Department of Anesthesiology, Shanghai General Hospital, Shanghai Jiao Tong University School of Medicine, Shanghai 200080, China
* Correspondence: edfeng@tongji.edu.cn

Received: 26 May 2026; Revised: 16 June 2026; Accepted: 22 June 2026; Published: 24 June 2026

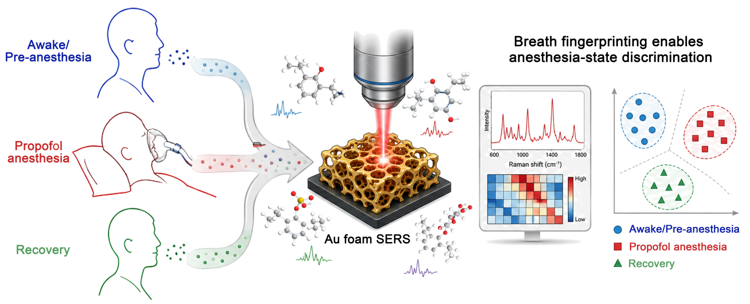

Abstract: Propofol anesthesia is commonly guided by hemodynamic signs, infusion parameters, and electroencephalography-derived indices, yet noninvasive molecular approaches for distinguishing anesthesia-related states remain limited. Here, we developed a mesoporous Au foam-based surface-enhanced Raman spectroscopy (SERS) chip for breath analysis of propofol metabolites signatures and anesthesia-state discrimination. The Au foam was fabricated by selective dealloying of Au-Ag alloy films, producing an interconnected ligament-pore architecture with a pore size of 55 nm and ligament width of 24 nm, which showed broad optical extinction near 785 nm, and strong SERS activity with an enhancement factor of approximately 6.84 × 10^5, as well as spatially uniform mapping over 30 × 30 μm^2, batch-to-batch reproducibility, humidity tolerance, 30-day storage stability, and resistance to breath-like gas flow. Using propofol, 4-hydroxypropofol, propofol glucuronide, and propofol sulfate as representative targets, molecule-specific SERS fingerprints and marker peaks were identified, enabling excellent discrimination of these structurally related molecules with classification accuracy above 85% with multivariate analysis. Quantitatively, all of these selected marker peaks showed linear responses over 2–75 ppb, with detection limits down to 0.663 ppb and spike recoveries above 90% in artificial breath matrix. Finally, breath SERS fingerprints collected from awake/pre-anesthesia, propofol anesthesia, and recovery states were analyzed by spectral scoring, PCA, supervised classification, and anesthesia-probability output, which achieved an overall state-discrimination accuracy of 86.7%, demonstrating the potential of mesoporous Au foam SERS chips for noninvasive molecular assessment of propofol anesthesia-related breath states. This work offered a compact optical strategy for molecularly informed assessment of propofol anesthesia-related breath signatures.

Keywords: mesoporous Au foam; surface-enhanced Raman scattering; exhaled breath analysis; propofol metabolites; anesthesia-state discrimination

1. Introduction

Propofol is one of the most widely used intravenous anesthetics for the induction and maintenance of general anesthesia because of its rapid onset, controllable hypnotic effect, and short recovery profile [1,2]. In clinical practice, propofol administration is commonly guided by infusion models, hemodynamic responses, and electroencephalography-derived indices [1–3]. However, these indirect parameters do not provide direct molecular information on the dynamic distribution, metabolism, and elimination of propofol during anesthesia. Blood-based drug monitoring can offer more accurate pharmacokinetic information, but repeated blood sampling is invasive, discontinuous, and incompatible with real-time perioperative decision-making. Therefore, developing a noninvasive analytical strategy capable of rapidly tracking propofol metabolites signatures would provide a valuable complement to conventional anesthesia monitoring.

Exhaled breath has emerged as an attractive matrix for noninvasive drug and metabolic monitoring because volatile and semi-volatile molecules can be continuously exchanged through the blood-air interface [4,5]. Previous studies have shown that propofol and volatile propofol-related species can be detected in exhaled breath during surgery, supporting the feasibility of breath-based monitoring of intravenous anesthesia [6–10]. Early real-time breath studies reported the detection of propofol and volatile metabolites, including 2,6-diisopropyl quinone and 2,6-diisopropyl phenol, in expired gases from patients undergoing surgery. More recent studies and reviews have further highlighted the potential of exhaled propofol monitoring using advanced analytical platforms such as proton-transfer-reaction mass spectrometry, selected-ion-flow-tube mass spectrometry, ion mobility spectrometry, secondary electrospray ionization high-resolution mass spectrometry, and gas chromatography-based techniques [6–12]. However, most breath-analysis technologies still rely on bulky instrumentation, complex ionization or separation modules, and specialized operating conditions, which limit their translation into compact, rapid, and real-time sensing formats.

Surface-enhanced Raman spectroscopy (SERS) provides a promising alternative for breath-based molecular detection because its molecular fingerprint specificity, high sensitivity, rapid optical readout, and compatibility with miniaturized instrumentation [13–16]. Unlike mass spectrometric methods that identify analytes by ion mass-to-charge ratios, SERS directly reports vibrational fingerprints of target molecules and their interfacial binding states, which is particularly attractive for detecting aromatic phenolic and quinone-like propofol metabolites. However, breath samples are highly humid, chemically complex, and contain target molecules at low concentrations [4,13,17]. Conventional planar noble-metal substrates often suffer from insufficient molecule capture, limited hotspot density, and poor reproducibility under gas-phase or high-humidity conditions. Therefore, a SERS interface specifically engineered for volatile molecule enrichment and stable signal amplification is needed.

Mesoporous gold structures offer a powerful materials platform for addressing limitations in breath samples analysis [18–22]. A well-established strategy of continuous mesoporous gold provided high surface area, abundant plasmonic nanogaps, tunable ligament/pore dimensions, and excellent chemical stability, which has been widely explored as a robust interface for molecular adsorption and a SERS substrate with electromagnetic enhancement, providing an attractive platform simultaneously as a molecular enrichment layer and a plasmonic hotspot scaffold [22–24].

Herein, we report a dealloyed mesoporous Au foam SERS chip for noninvasive breath analysis of propofol metabolites signatures and anesthesia-state discrimination (Scheme 1). The chip was prepared by selective dealloying of Au-Ag alloy films, producing a three-dimensional interconnected Au ligament–pore network with tunable structural parameters and broad optical extinction near the 785 nm Raman excitation wavelength, which provided a robust breath-compatible SERS interface, combining strong 4-mercaptobenzonitrile (4-MBN) enhancement, homogeneous signal distribution, batch reproducibility, humidity tolerance, storage stability, and resistance to breath-like gas flow. The Au foam-enhanced fingerprints enabled reliable multivariate discrimination of structurally related propofol species, with supervised classification achieving an accuracy above 85%. In artificial breath matrix, the selected marker peaks exhibited linear ppb-level responses over 2–75 ppb with low detection limits of 0.663–1.259 ppb, and spike recoveries above 90%, confirming the analytical reliability of the platform under breath-relevant conditions. Finally, breath SERS fingerprints from awake/pre-anesthesia, propofol anesthesia, and recovery states were analyzed through composite spectral scoring, PCA, supervised classification, and anesthesia-state probability output, achieving an overall state-discrimination accuracy of 86.7%, which can identify awake/pre-anesthesia and propofol anesthesia states with accuracies of 93.3% and 90.0%, respectively. This work demonstrated a mesoporous Au foam SERS interface that integrated breath-compatible molecular enrichment, ppb-level detection, and state discrimination, offering a compact optical strategy for molecularly informed assessment of propofol anesthesia-related breath signatures.

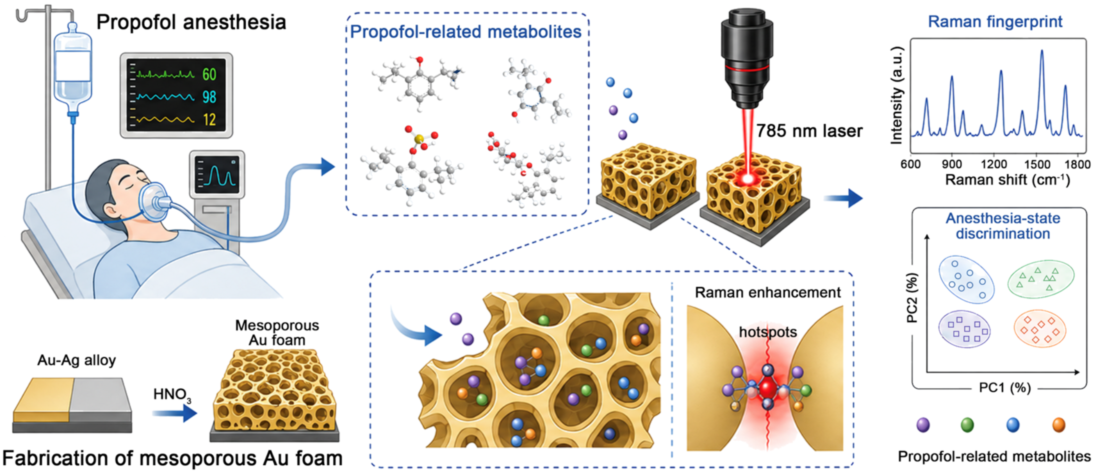

Scheme 1. Mesoporous Au foam-based SERS platform for propofol-related metabolites in exhaled breath detection.

2. Experimental Section

2.1. Fabrication of Mesoporous Au Foam Chips

Mesoporous Au foam chips were fabricated by selective dealloying of Au-Ag alloy films. Briefly, Si/SiO_2 substrates were sequentially cleaned by sonication in acetone, ethanol, and ultrapure water, followed by drying under a nitrogen stream. Au-Ag alloy films were then deposited onto the cleaned substrates by magnetron sputtering. The obtained Au-Ag alloy films were immersed in nitric acid solution to selectively remove Ag and generate an interconnected porous Au network. The dealloying time was varied to tune the porous structure, giving Au foam samples dealloyed for 5, 15, and 30 min. After dealloying, the chips were thoroughly rinsed with ultrapure water and ethanol to remove residual acid and dissolved metal ions, and then dried under nitrogen.

2.2. Structural and Compositional Characterization

The morphology of the Au-Ag alloy films and dealloyed Au foam chips was characterized by field-emission scanning electron microscopy (Zeiss GeminiSEM 300, Carl Zeiss Microscopy GmbH, Jena, Germany) operated at an accelerating voltage of 3–5 kV. Transmission electron microscopy (TEM), high-resolution TEM (HRTEM), high-angle annular dark-field scanning TEM (HAADF-STEM), and energy-dispersive X-ray spectroscopy (EDS) mapping were performed on a JEM-2100F transmission electron microscope (JEOL, Tokyo, Japan). Atomic force microscopy (AFM) was performed using a Dimension Icon AFM system (Bruker, Billerica, MA, USA) in tapping mode under ambient conditions. Nitrogen adsorption-desorption measurements were conducted on a Micromeritics ASAP 2460 surface area and porosity analyzer (Micromeritics, Norcross, GA, USA) at 77 K. X-ray diffraction (XRD) patterns were recorded using an X-ray diffractometer (SmartLab, Rigaku, Tokyo, Japan) equipped with a Cu Kα radiation source ($\lambda = 1.5406$ Å). The diffraction data were collected over a 2θ range of 30–90° at a scanning rate of 2–5° min^{-1}. X-ray photoelectron spectroscopy (XPS) was performed on an ESCALAB 250Xi spectrometer (Thermo Fisher Scientific, Waltham, MA, USA) using a monochromatic Al Kα X-ray source ($h\nu = 1486.6$ eV). UV-vis-NIR extinction spectra of the Au-Ag alloy and Au foam substrates were recorded using a UV-vis-NIR spectrophotometer (UV-3600, Shimadzu, Kyoto, Japan) over the wavelength range of 400–1000 nm. The optical extinction around the 785 nm Raman excitation wavelength was specifically analyzed to evaluate the plasmonic compatibility of the Au foam substrate for SERS measurements. Raman and SERS spectra were collected using a confocal Raman microscope (Renishaw inVia, Renishaw plc, Wotton-under-Edge, Gloucestershire, UK) equipped with a 785 nm diode laser. The laser was focused onto the sample surface through a 50× objective lens. The laser power at the sample surface was controlled at 1 mW. The spectral acquisition time was 10 s, and each spectrum was accumulated 3 times.

2.3. 4-MBN Modification and SERS Performance Evaluation

4-MBN was used as a standard Raman reporter to evaluate the SERS activity of the Au foam substrates. Before modification, the Au foam chips were rinsed sequentially with ethanol and ultrapure water, dried under a nitrogen stream, and treated by UV-ozone for 10 min to remove possible organic contaminants. A 4-MBN stock solution was prepared in ethanol and diluted to a working concentration of 1 mM. The cleaned Au foam chips were immersed in the 4-MBN ethanol solution at room temperature for 12 h. After incubation, the chips were thoroughly rinsed with ethanol three times to remove physically adsorbed or unbound 4-MBN molecules, followed by drying under nitrogen. The obtained 4-MBN-modified Au foam chips were used immediately for SERS measurements or stored in a dry container before testing.

2.4. SERS Detection of Propofol Metabolites

Propofol, 4-hydroxypropofol, propofol glucuronide, and propofol sulfate were selected as representative propofol metabolites for SERS fingerprint analysis. Stock solutions of each compound were prepared in ethanol or ethanol/water mixed solvent depending on molecular solubility. For propofol and 4-hydroxypropofol, ethanol was used as the primary solvent. For propofol glucuronide and propofol sulfate, ethanol/water mixed solvent was used to improve dissolution. Before SERS measurement, the stock solutions were diluted to the desired working concentrations. For molecular fingerprint acquisition, the optimized Au foam chips were first rinsed with ethanol and ultrapure water, dried under nitrogen, and then exposed to the target molecular solution. Typically, 20–50 µL of the target solution was dropped onto the Au foam surface and incubated at room temperature for 10–30 min to allow molecular adsorption into the porous Au network. After incubation, the chip was gently rinsed with the corresponding solvent to remove excessive unbound molecules and dried under nitrogen. Blank Au foam chips treated with solvent alone were measured as background controls.

2.5. Artificial Breath Preparation and Gas-Phase SERS Calibration

Artificial breath matrix was prepared to simulate the humid gas environment of exhaled breath. Briefly, carrier gas was passed through a humidification chamber containing ultrapure water to generate humidified gas. The relative humidity was adjusted by controlling the humidification temperature and gas-flow ratio. For matrix-matched calibration experiments, known amounts of propofol metabolites were introduced into the artificial breath stream to generate ppb-level vapor or aerosol-associated standards. The concentration range was set as 0, 2, 5, 10, 20, 35, 50, and 75 ppb, covering the breath-relevant low-concentration range.

For each measurement, the artificial breath containing the target molecule was directed onto the optimized Au foam SERS chip for 5 min, to allow molecular adsorption/enrichment within the porous Au foam. After exposure, the chip was immediately transferred to the Raman microscope for SERS measurement. The same Raman acquisition parameters were used throughout the calibration experiments.

2.6. Spike-Recovery Experiments in Artificial Breath Matrix

Spike-recovery experiments were performed to evaluate the quantitative accuracy of the Au foam SERS platform in artificial breath matrix. Propofol, 4-hydroxypropofol, propofol glucuronide, and propofol sulfate were individually spiked into artificial breath matrix at 10 ppb. The spiked artificial breath was introduced onto the Au foam chip under the same gas-exposure conditions used for calibration. After exposure, SERS spectra were collected, and the corresponding marker peak intensities were extracted. The measured concentration of each target molecule was calculated from its matrix-matched calibration curve. The recovery rate was calculated according to:

$$\text{Recovery (\%)} = C_{\text{found}}/C_{\text{spiked}} \times 100\%$$

where C_{found} is the calculated concentration from the calibration curve and C_{spiked} is the spiked concentration.

2.7. Anti-Interference Evaluation under Breath-Relevant Conditions

To evaluate the selectivity and anti-interference capability of the Au foam SERS platform, common breath-related volatile compounds were introduced into the artificial breath matrix. The tested interferents included acetone, ethanol, isoprene, ammonia, acetaldehyde, and a mixture of these interferents. High-humidity mixed-interferent conditions were also tested by introducing the interferent mixture into artificial breath at 95% relative humidity. For each anti-interference experiment, the target molecule was maintained at a fixed concentration, while the interferent was introduced into the artificial breath stream. The signal retention of each marker peak was calculated as:

$$\text{Signal retention (\%)} = I_{\text{interferent}}/I_{\text{control}} \times 100\%$$

where $I_{\text{interferent}}$ is the marker peak intensity measured in the presence of interferents, and I_{control} is the marker peak intensity measured in artificial breath without interferents.

2.8. Breath Sample Collection and Au Foam SERS Analysis

This study was approved by the Ethics Committee of Shanghai First People's Hospital, with the approval number 2025-192. Basic demographic and clinical information of the enrolled patients, including age, gender, ASA physical status, surgical type, and anesthesia protocol. Breath samples were collected from three anesthesia-related states: awake/pre-anesthesia, propofol anesthesia, and recovery. Breath samples were collected using a breath sampling device. The exhaled breath was transferred and directed onto the Au foam chip for molecular adsorption and enrichment for 30 min. After breath exposure, the Au foam chip was immediately subjected to Raman measurement. SERS spectra were collected in the 600–1800 cm^{-1} fingerprint region.

It should be noted that awake/pre-anesthesia samples were collected before propofol administration, anesthesia-state samples were collected after a stable propofol anesthesia condition was reached, and recovery samples were collected after discontinuation of propofol during the recovery period. Patients with severe respiratory disease, severe hepatic or renal dysfunction, active infection, metabolic disorders, recent alcohol intake, or other conditions that could markedly influence breath VOC profiles were excluded.

2.9. Breath SERS Score Calculation

For breath-state analysis, the integrated areas of four propofol-related spectral regions were extracted from each breath spectrum: 842 cm^{-1} region, 1048–1088 cm^{-1} region, 1452 cm^{-1} region, and 1600 cm^{-1} region. Each regional area was normalized across all breath samples. A composite breath SERS score was then calculated by averaging the normalized integrated areas:

$$\text{Breath SERS score} = (I_{842} + I_{1048\text{–}1088} + I_{1452} + I_{1600})/4$$

where I represents the normalized integrated area of each selected spectral region.

2.10. PCA and Classification Analysis

Principal component analysis was performed to visualize the unsupervised separation of breath SERS fingerprints from different anesthesia-related states. Input features included the integrated areas and peak intensities of the selected propofol-related spectral regions. Before PCA, all features were standardized to zero mean and unit variance. The first two principal components were used to construct the PCA score plot. Meanwhile, supervised classification was performed using a random forest (RF) classifier. The input features were manually selected based on the assigned Raman marker peaks and propofol-related spectral regions. For molecular-standard classification, representative marker-peak intensities were used as input features. For breath-state classification, the integrated areas and peak intensities of selected spectral regions were extracted. The dataset was divided into training and testing sets using a stratified strategy to maintain class balance. Five-fold cross-validation was performed within the training set for model optimization, and the independent testing set was used for final evaluation.

3. Results and Discussion

3.1. Fabrication and Structural Characterization of Dealloyed Mesoporous Au Foam Chips

To construct a plasmonically active interface for breath-based SERS detection, mesoporous Au foam chips were fabricated through a dealloying strategy using Au-Ag alloy films as sacrificial precursors. As schematically illustrated in Figure 1A, the morphological evolution of the Au foam was first examined by scanning electron microscopy. The pristine Au-Ag alloy film exhibited a relatively compact and continuous surface, without obvious nanoscale porosity. After dealloying, a distinct porous morphology was clearly observed, confirming the successful transformation from a dense alloy film into an interconnected Au foam structure (Figure 1B). The dealloyed Au foam displayed a continuous ligament-pore network over a large area, indicating that selective Ag removal occurred uniformly across the film. By adjusting the dealloying time, the pore structure could be systematically regulated. As displayed in Figure S1, the Au foam sample dealloyed for 5 min showed small and densely distributed pores with an average pore size of approximately 24 ± 6 nm and a ligament width of approximately 13 ± 3 nm, suggesting an early-stage dealloying structure with fine Au ligaments but partially developed pore channels. With the dealloying time extended to 15 min, Au foam exhibited a more open and well-connected porous network, with an average pore size of approximately 55 ± 9 nm and a ligament width of approximately 24 ± 4 nm. This structure provided a favorable balance between accessible pores for molecule diffusion and nanoscale Au ligaments for plasmonic hotspot generation. Further prolonging the dealloying time to 30 min led to obvious coarsening of the porous framework, giving enlarged pores of approximately 105 ± 18 nm and thicker ligaments of approximately 42 ± 6 nm. Such ligament coarsening reduced the density of nanoscale junctions and narrow interligament gaps, which are critical for electromagnetic field localization. Thus, the Au foam with deallying time 15 min sample was selected as the optimized substrate because it preserved a continuous Au ligament network with moderate ligament width while providing sufficiently open pores for volatile-molecule access. Moreover, as shown in Figure 1C, the porous Au layer was continuously attached to the Si/SiO_2 substrate with a depth of 330 nm, suggesting good structural integrity after dealloying. Transmission electron macroscopy (TEM) image revealed that the Au foam consisted of interconnected nanoscale ligaments and open pores, which was consistent with the SEM results (Figure 1D). The high-resolution TEM image displayed clear lattice fringes with an interplanar spacing of approximately 0.235 nm, which can be assigned to the Au (111) plane, confirming the crystalline nature of the dealloyed Au ligaments. In addition, The High-angle annular dark-field (HAADF) image and corresponding energy dispersive spectrometer (EDS) mapping showed that Au was continuously distributed throughout the porous ligament network, whereas the Ag signal was greatly weakened after dealloying, indicating efficient removal of Ag from the precursor alloy film (Figure 1E). In addition to electron microscopy, atomic force microscopy (AFM) analysis further quantified the roughness evolution associated with dealloying (Figure S2). The Au-Ag alloy precursor showed a relatively smooth surface with low arithmetic average roughness (Ra) and root-mean-square roughness (Rq) <5 nm. In contrast, the Au foam displayed a significant increase in roughness with Ra and Rq values reaching approximately 17.5 nm and 22.0 nm, respectively, indicating the presence of nanoscale protrusions and recessed pore structures across the dealloyed surface, which was consistent with the SEM observation.

To further support the porous nature of the Au foam, Brunauer-Emmett-Teller (BET) nitrogen adsorption-desorption analysis was performed. As shown in Figure S3, The Au foam showed a type-IV-like adsorption–desorption isotherm with an apparent hysteresis loop, indicating the presence of accessible mesoporous/macroporous channels. The BET surface area was approximately 21–22 $m^2\ g^{-1}$, and the total pore volume was approximately 0.292 $cm^3\ g^{-1}$. The BJH pore-size distribution showed a dominant pore-size peak centered at approximately 55 nm, together with a smaller shoulder around 23–26 nm, which was consistent with the SEM-derived average pore diameter of Au foam. The smaller shoulder may originate from pore throats and nanoscale channels within the interconnected Au foam network.

Furthermore, as shown in Figure 1F, the dealloyed samples exhibited characteristic X-ray diffraction (XRD) pattern corresponding to face-centered cubic Au, including Au (111), Au (200), Au (220), and Au (311). Compared with the Au-Ag alloy precursor, the diffraction peaks of the dealloyed Au foam shifted toward the standard Au positions, further supporting the removal of Ag and the formation of an Au-rich porous framework. The high-resolution X-ray photoelectron spectroscopy (XPS) survey spectra provided additional evidence for the compositional change. As displayed in Figure 1G, in the Au-Ag alloy precursor, the dominant Au-related signals were observed at approximately 84.0 and 87.7 eV, corresponding to Au $4f_{7/2}$ and Au $4f_{5/2}$, respectively, confirming the metallic Au state in the alloy film. The alloy precursor also exhibited characteristic Ag peaks, including Ag $3d_{5/2}$ and Ag $3d_{3/2}$ at approximately 368.2 and 374.2 eV. After dealloying, the Au 4f doublet remained clearly visible, no obvious positively shifted Au oxide peak was observed in the survey spectra, supporting the chemical stability of the dealloyed Au foam. While the Ag 3d signals were markedly weakened, indicating the selective removal of Ag from the alloy matrix and the formation of an Au-rich porous framework.

The optical response of the Au foam chips was then evaluated by UV-vis-NIR spectroscopy (Figure 1H). Compared with the relatively smooth Au-Ag alloy precursor, the dealloyed Au foam exhibited a broad extinction response across the visible to near-infrared region centered at ~700 nm, which can be attributed to the interconnected Au ligament network, nanoscale curvature, and heterogeneous pore geometry. Importantly, the Au foam maintained strong optical extinction around the commonly used Raman excitation wavelength of 785 nm, enabling sufficient SERS activity towards standard Raman reporter 4-MBN which can be stably anchored on Au through Au-S bonding. As shown in Figure S4, 4-MBN exhibited characteristic Raman bands of ring vibration modes at approximately 1589 cm^{-1}, together with a distinct nitrile stretching band near 2222 cm^{-1} [25,26]. Compared with the Si/SiO_2, the dealloyed Au foam chips showed dramatically enhanced 4-MBN signals with a enhancement factor about 6.84×10^5, confirming the formation of abundant SERS-active sites after dealloying. Collectively, the dealloyed Au foam offers an optimized SERS-active interface for converting weak surface-bound molecular vibrations into clearly distinguishable Raman fingerprints, providing the analytical foundation for subsequent breath detection of propofol-related species.

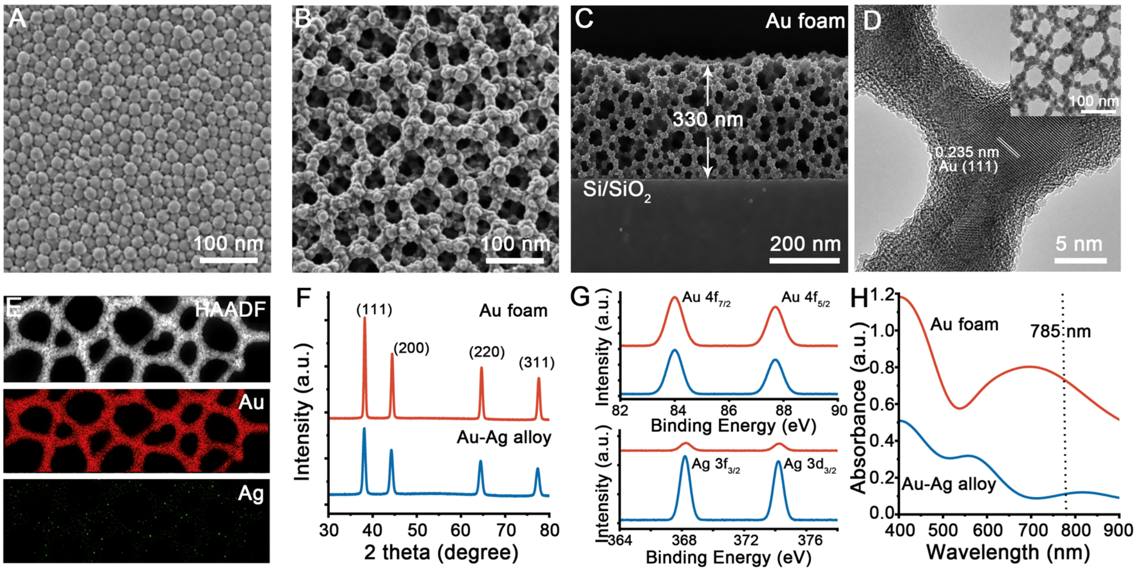

Figure 1. (**A**,**B**) SEM images of (**A**) Au-Ag alloy and (**B**) Au foam. (**C**) SEM side view of Au foam platform, (**D**) High resolution TEM image of Au foam, inset: TEM image of Au foam. (**E**) EDS mapping of Au foam. (**F**) XRD pattern of Au-Ag alloy and Au foam. (**G**) XPS spectra of Au 4f and Ag 3d on Au foam. (**H**) UV-Vis spectra of Au-Ag alloy and Au foam.

3.2. SERS Performance and Stability of Optimized Au Foam Substrates

Further SERS performance comparison was performed Figure 2A. All 4-MBN-modified substrates displayed two characteristic Raman bands, which were similar with Au foam. Significantly, compared with the flat Au substrate and the undealloyed Au-Ag alloy film, the dealloyed Au foam substrates generated much stronger SERS signals, confirming that the porous Au architecture formed during dealloying effectively enhanced the Raman scattering of 4-MBN. Moreover, as quantified in Figure 2B, the Au foam dealloyed for 15 min showed the highest 2226 cm^{-1} intensity among all tested substrates, whereas the Au foam dealloyed for 5 min and 30 min produced weaker responses, which was consistent with the structural evolution described above. Specifically, the 5 min dealloyed Au foam contained relatively small pores, which may limit molecular accessibility to the inner porous network. In contrast, prolonged dealloying for 30 min resulted in enlarged pores and coarsened ligaments, reducing the density of nanoscale junctions and plasmonic hotspots. Moreover, the Au foam dealloyed for 15 min exhibited the highest enhancement factor among the representative Au foam substrates, further confirming that the intermediate dealloying condition produced the most effective SERS-active structure (Figure 2C).

Furthermore, SERS mapping was performed on the Au foam substrate using the 2226 cm^{-1} peak intensity as the readout signal to evaluate the spatial signal uniformity. As shown in Figure 2D, the mapping image collected over a 30 × 30 μm^2 area displayed a relatively homogeneous signal distribution without large inactive regions. The corresponding intensity distribution histogram further showed that the measured intensities were concentrated within a narrow range (RSD≈9%), which can be attributed to the continuous three-dimensional Au ligament network, providing distributed SERS-active sites rather than isolated hotspots. In addition, the signal reproducibility of the optimized Au foam substrate was further evaluated under different breath-relevant atmospheres. As shown in Figure 2E, the 2226 cm^{-1} signal remained relatively stable under dry N$_2$, different relative humidity conditions, and artificial breath. Although a slight decrease in signal intensity was observed under high-humidity and artificial breath conditions, the overall SERS response was well preserved, suggesting that the Au foam substrate can maintain stable molecular readout in humid environments, which is essential for subsequent breath analysis. Similarly, the 2226 cm^{-1} intensity showed only moderate attenuation during high-humidity exposure to 95% RH for different durations, indicating that the 4-MBN-modified Au foam retained its SERS activity under prolonged humid conditions, which is likely associated with the chemical inertness of the Au-dominant framework and the open porous structure (Figure 2F).

As shown in Figure 2G, the 2226 cm^{-1} intensities obtained from different batches remained comparable, demonstrating good batch-to-batch reproducibility of the dealloying-based fabrication strategy (RSD < 2.5%). Meanwhile, the long-term storage stability of the optimized Au foam substrate was also investigated in Figure 2H, the 2226 cm^{-1} signal was largely retained over 30 days of storage with only a gradual decrease in intensity. Finally, as shown in Figure 2I, the SERS signal showed only a moderate decrease after repeated flow exposure, indicating that the Au foam substrate can withstand gas flushing without severe signal loss.

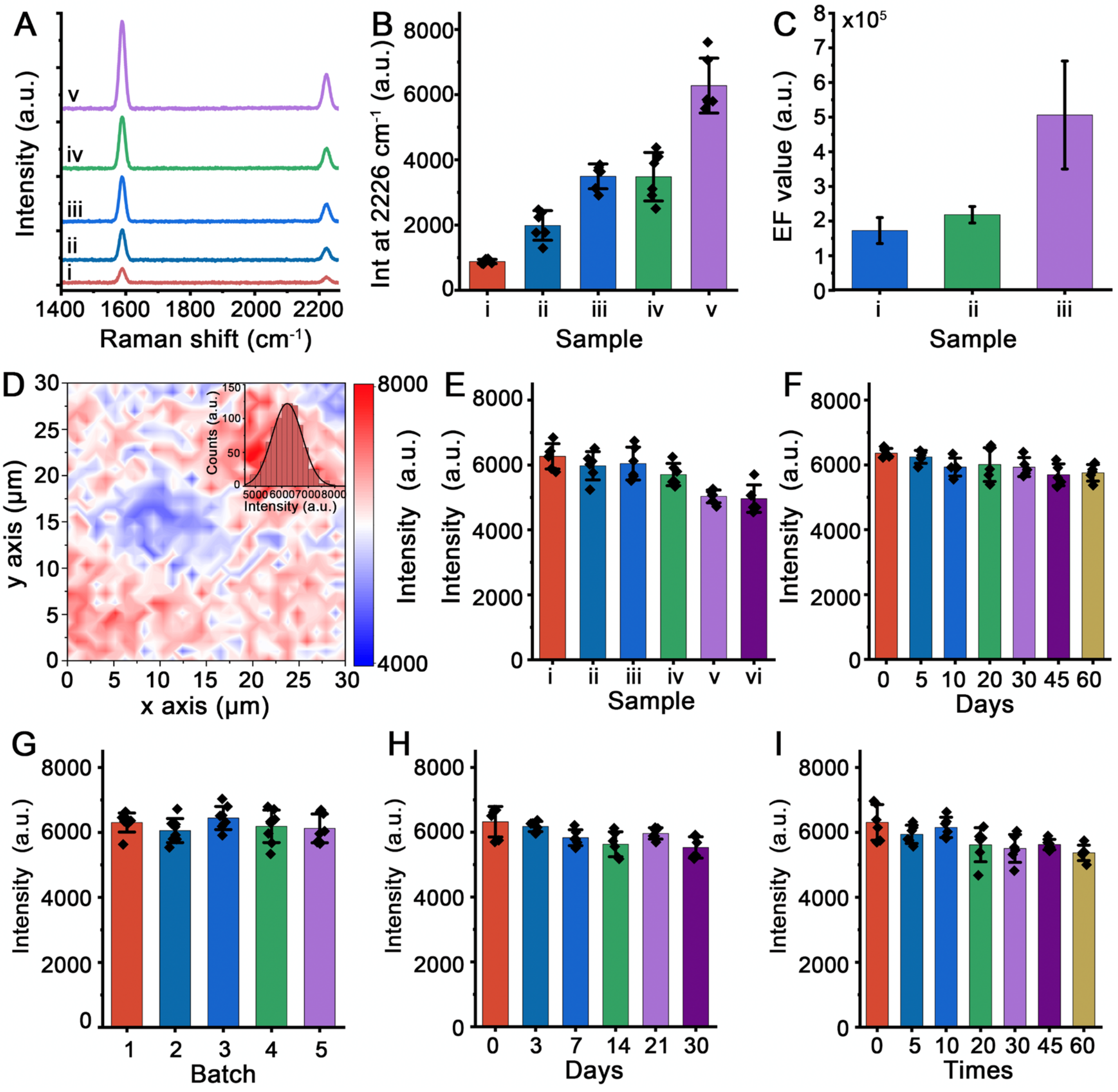

Figure 2. (**A**) Representative SERS spectra of 4-MBN collected from different substrates (i) flat Au substrate, (ii) Au-Ag alloy; (iii) Au foam dealloyed for 5 min; (iv) Au foam dealloyed for 30 min; (v) Au foam dealloyed for 15 min. (**B**) Quantitative comparison of the 2226 cm^{-1} peak intensity among samples in Figure 2A. (**C**) Calculated SERS enhancement factor values based on the 2226 cm^{-1} C≡N stretching band of 4-MBN for representative samples, Au foam dealloyed for (i) 5 min; (ii) 30 min; (iii) 15 min. (**D**) SERS mapping image of the optimized Au foam substrate based on the 2226 cm^{-1} peak intensity over a 30 × 30 μm^2 area. Inset: the corresponding intensity distribution histogram. (**E**) Signal reproducibility of the Au foam substrate measured under different breath atmosphere (i) dry N_2, (ii) 40% RH, (iii) 60% RH, (iv) 80% RH, (v) 95% RH, (vi) artificial breath. (**F**) SERS signal stability under 95% RH conditions storage for different days. (**G**) Batch-to-batch reproducibility of five independently prepared Au foam substrates. (**H**) Storage stability of the Au foam substrate over 30 days. (**I**) Signal retention after repeated breath-like gas flow exposure for different times. Error bars represent standard deviations from repeated measurements.

3.3. SERS Fingerprint Discrimination of Propofol Metabolites

To further investigate the resolve molecular fingerprints ability associated with propofol metabolism, a representative propofol metaboliteslibrary was established, including propofol, 4-hydroxypropofol, propofol glucuronide, and propofol sulfate, which were selected to represent the parent anesthetic molecule together with structurally related oxidative and conjugated products [27,28]. As shown in Figure 3A, propofol, 4-hydroxypropofol, propofol glucuronide, and propofol sulfate were selected as representative propofol-related model analytes, which covered the major structural categories involved in propofol biotransformation, including the parent drug, oxidative aromatic hydroxylation product, O-glucuronide conjugate, and O-sulfate conjugate. Figure S5 indicated that the SERS signal increased rapidly during the initial exposure stage and reached a near-plateau after approximately 5 min, indicating that the adsorption/enrichment of propofol metabolites on the mesoporous Au foam substrate had approached a stable state. As shown in Figure 3B, the blank Au foam substrate showed only weak background signals, whereas propofol, 4-hydroxypropofol, propofol glucuronide, and propofol sulfate all produced clear and distinguishable SERS spectra. For propofol, the band at 755 cm^{-1} was tentatively assigned to aromatic ring deformation coupled with isopropyl-related vibration, while the peak at 1008 cm^{-1} was attributed to aromatic ring breathing. The bands at 1178 and 1266 cm^{-1} were assigned to phenolic C-O stretching and C-H in-plane bending vibrations. The strong peak at 1452 cm^{-1} was associated with C-H bending from the isopropyl groups, and the band at 1602 cm^{-1} was attributed to aromatic C=C stretching.

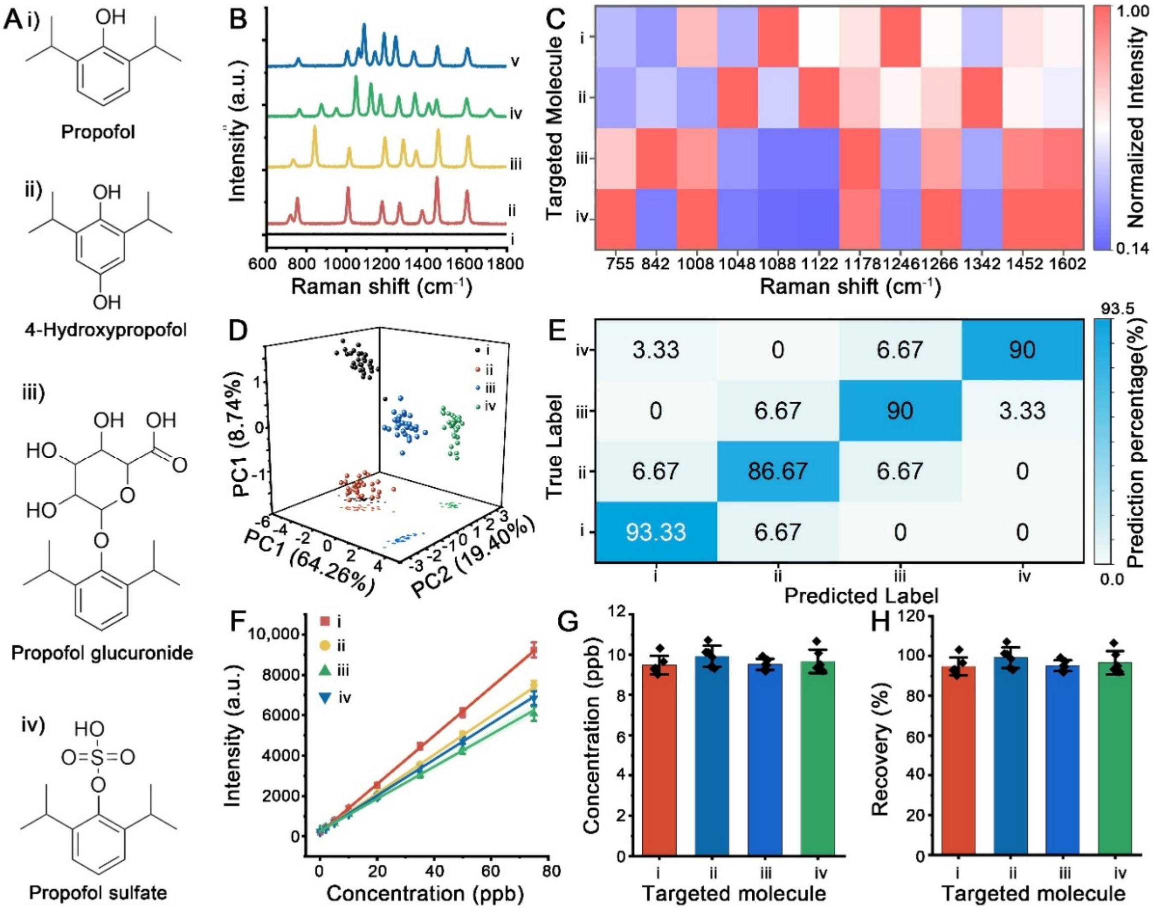

Figure 3. SERS fingerprint discrimination and ppb-level artificial-breath validation of propofol metabolites on the optimized Au foam substrate. (**A**) Chemical structures of the selected propofol metaboliteslibrary: (i) propofol, (ii) 4-hydroxypropofol, (iii) propofol glucuronide, and (iv) propofol sulfate. (**B**) Representative SERS spectra collected on the optimized Au foam substrate, including (i) blank Au foam and the four target molecules (ii) propofol, (iii) 4-hydroxypropofol, (iv) propofol glucuronide, and (v) propofol sulfate. (**C**) Heatmap of selected Raman features extracted from the SERS spectra. (**D**) PCA score plot based on selected SERS features (n = 30). (**E**) Row-normalized confusion matrix for supervised classification of the target molecules using selected Raman features (n = 30). (**F**) Matrix-matched calibration curves of the four target molecules in artificial breath matrix at ppb-level concentrations (n = 5). (**G**) Calculated concentrations of 10 ppb spiked target molecules in artificial breath matrix (n = 5). (**H**) Corresponding spike recovery rates of the four target molecules in artificial breath matrix (n = 5). Unless otherwise indicated, labels i–iv correspond to propofol, 4-hydroxypropofol, propofol glucuronide, and propofol sulfate, respectively.

Compared with propofol, 4-hydroxypropofol exhibited altered relative intensities and additional hydroxylation-sensitive features. In particular, the band around 842 cm^{-1} became more prominent, which may be associated with hydroxylation-induced changes in aromatic ring deformation and C-O-related vibrations. The enhanced features near 1192, 1284, 1458, and 1608 cm^{-1} further indicate that the introduction of an additional hydroxyl group changes the local vibrational environment of the aromatic ring. Additionally, propofol glucuronide displayed a different spectral pattern with characteristic bands around 1048, 1122, 1170, 1260, and 1342 cm^{-1}, which can be attributed mainly to C-O, C-O-C, and glycosidic-bond-related vibrations from the glucuronide moiety, and coupled aromatic vibrations from the propofol skeleton. Meanwhile, propofol sulfate showed pronounced features around 1088, 1188, and 1246 cm^{-1}, consistent with sulfate-associated vibrations and substituent-sensitive aromatic modes. These peak assignments suggest that although the four molecules share a related aromatic framework, their peripheral metabolic modifications introduce distinct vibrational signatures that can be captured by the Au foam SERS substrate (Table S1).

Furthermore, a set of representative Raman features was extracted to construct a feature-intensity heatmap (Figure 3C). The intensity of each Raman feature was normalized to the maximum value among the target molecules, allowing direct comparison of the relative contribution of each feature to molecular discrimination, clearly showing that propofol was characterized by strong aromatic and phenolic features, 4-hydroxypropofol by hydroxylation-sensitive vibrations, propofol glucuronide by C-O/C-O-C-dominated features, and propofol sulfate by sulfate-associated vibrations. Typically, several molecule-specific bands with high intensity and low spectral overlap were identified as candidate quantitative marker peaks, including 1452 cm^{-1} for propofol, 842 cm^{-1} for 4-hydroxypropofol, 1048 cm^{-1} for propofol glucuronide, and 1088 cm^{-1} for propofol sulfate. PCA was then performed using the selected SERS features to evaluate the discrimination ability towards these propofol metabolites in an unsupervised manner. As shown in Figure 3D, the four target molecules formed distinguishable clusters in the PCA score space. The PC1, PC2 and PC3 were explained 64.3%, 19.4% and 8.74% of the total variance, respectively, accounting for 100% of the spectral variance in combination, suggesting that differences in the Au foam-enhanced SERS fingerprints are sufficient to differentiate propofol and its related molecular derivatives. To further assess the classification capability of the SERS fingerprints, a supervised classification model was trained using the selected Raman features [29,30]. The row-normalized confusion matrix shown in Figure 3E demonstrated accurate classification of the four propofol metabolites using a balanced test set containing 30 spectra per class. The overall classification accuracy reached over 85%, indicating that the spectral differences observed in the SERS fingerprints could be translated into reliable molecular recognition.

Moreover, as shown in Figures S6 and S7, common breath-related interferents, including acetone, ethanol, isoprene, ammonia, acetaldehyde, mixed interferents, and high-humidity mixed interferents, caused only limited signal variation in the molecule-specific marker peaks. The propofol-related marker signals were largely retained under single-interferent conditions, and remained detectable over 80%, even in the presence of mixed interferents and 95% RH background, indicating the suitability for subsequent artificial-breath and real-breath analysis.

Furthermore, matrix-matched calibration curves were established at ppb-level concentrations. As shown in Figure 3F, the SERS intensities of these marker peaks increased linearly with concentration over the tested range of 2–75 ppb with an excellent limit of detection (LOD) of 0.847 ppb for propofol, 0.663 ppb for 4-hydroxypropofol, 1.259 ppb for propofol glucuronide and 1.035 ppb for propofol sulfate, respectively, demonstrating that the optimized Au foam substrate enabled sensitive ppb-level quantification of propofol metabolites, which can be reliably used for concentration estimation in breath-relevant environments (Table S2). Then, spike-recovery experiments were further performed at 10 ppb to assess quantitative accuracy. As shown in Figure 3G,H, the calculated concentrations were close to the spiked values, and the recovery rates remained >90%, which was also observed across different concentration levels (Figure S8), confirming the reliability of the Au foam SERS platform for ppb-level detection in artificial breath, which showed better performance than reported works before (Table S3).

3.4. Breath SERS Fingerprinting for Discrimination of Propofol Anesthesia-Related States

As illustrated in Figure 4A, exhaled breath samples were collected from three representative physiological states, including awake/pre-anesthesia, propofol anesthesia, and recovery (Table S4). The collected breath samples were introduced onto the optimized Au foam SERS chip, followed by Raman spectral acquisition, feature extraction, and state discrimination. Representative breath SERS spectra from the three states are shown in Figure 4B. Unlike the standard-molecule spectra, the breath spectra displayed several broader bands, shoulder peaks, reflecting the complex molecular composition of exhaled breath. Compared with the relatively weak and broad spectral profile observed in the awake/pre-anesthesia state, the propofol anesthesia state exhibited enhanced SERS features in several spectral regions around 842, 1048–1088, 1452, and 1600 cm^{-1}, which exhibited high corelationship towards the Raman features previously identified from propofol-related standards. Moreover, the recovery-state spectrum showed an intermediate pattern, in which the propofol-related spectral features were still observable but attenuated compared with the anesthesia state, suggesting that the Au foam substrate can capture anesthesia-associated molecular changes from complex breath backgrounds.

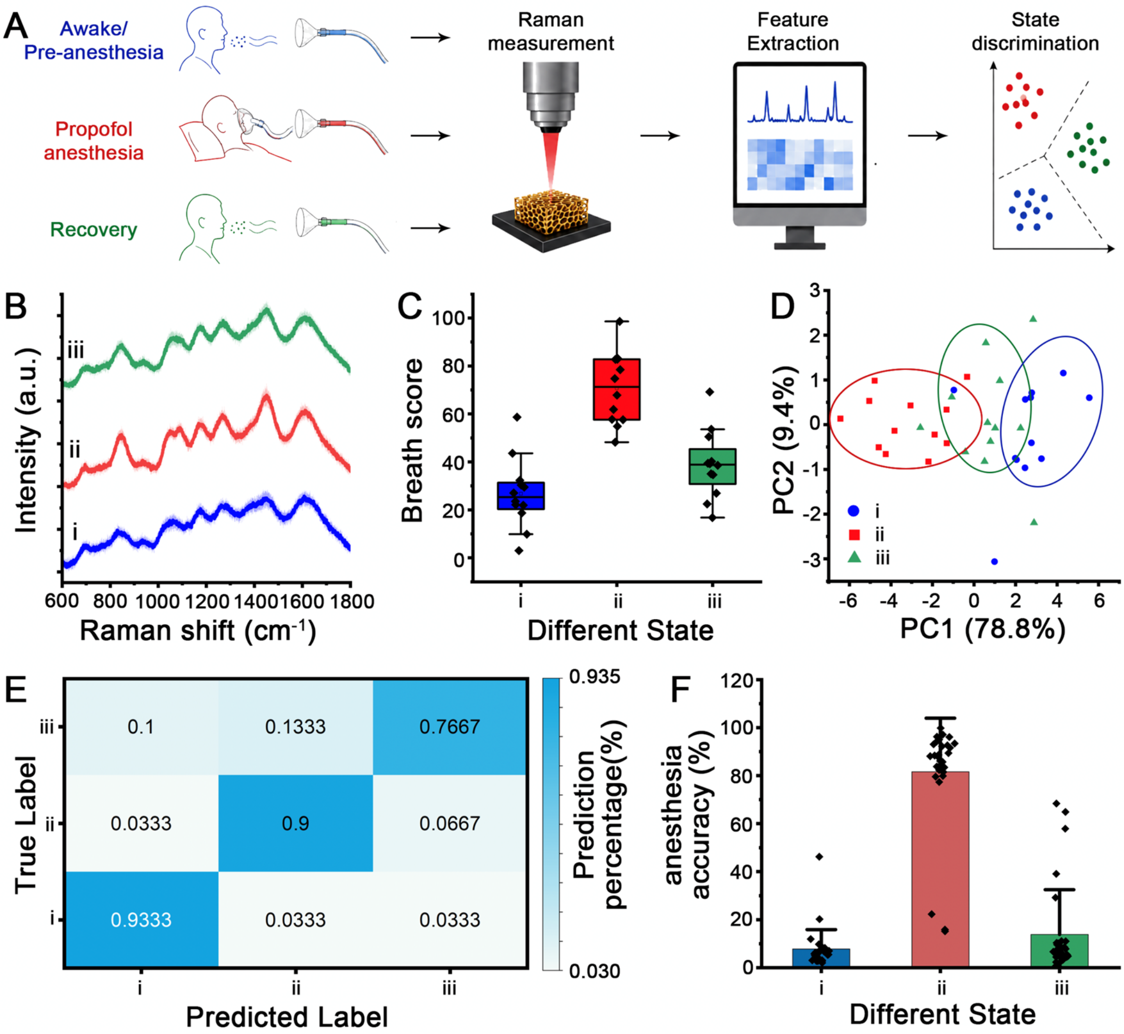

Figure 4. Breath SERS fingerprinting for discrimination of propofol anesthesia-related states. (**A**) Schematic workflow for breath-based anesthesia-state discrimination using the Au foam SERS platform. (**B**) Representative breath SERS spectra collected from the three states. (**C**) Distribution of breath SERS scores calculated from selected propofol-related spectral regions. (**D**) PCA score plot of breath SERS fingerprints. (**E**) Row-normalized confusion matrix for supervised classification of the three breath states using SERS-derived features (n = 30). (**F**) Predicted anesthesia-state probability extracted from the same classification. Unless otherwise indicated, labels i–iii correspond to awake/pre-anesthesia, propofol anesthesia, and recovery, respectively.

To quantitatively summarize the changes in these propofol-related spectral regions, a breath SERS score was calculated by integrating areas of the 842, 1048–1088, 1452, and 1600 cm^{-1} regions, which were first normalized and then averaged to generate a composite score. As shown in Figure 4C, the breath SERS score was significantly elevated in the propofol anesthesia group compared with the awake/pre-anesthesia group, while the recovery group showed a decreased score relative to the anesthesia group, which is consistent with the spectral changes observed before, indicating that the selected spectral regions collectively reflect anesthesia-associated breath molecular signatures. Subsequently, PCA analysis in an unsupervised manner was performed to evaluate the distinguish ability on different anesthesia-related states using the breath SERS fingerprints. As shown in Figure 4D, the awake/pre-anesthesia, propofol anesthesia, and recovery samples formed distinguishable clusters in the PCA score space. PC1 explained 78.8% of the total variance, whereas PC2 explained 9.4%, indicating that the major spectral variance was associated with state-dependent differences in the breath SERS fingerprints. Importantly, the anesthesia group was separated from the awake/pre-anesthesia group, while the recovery group was positioned between or partially overlapping with the other two states, consistent with a transitional molecular profile during recovery from anesthesia.

To further assess the state-discrimination capability of the SERS fingerprints, a supervised classification model was constructed using SERS-derived spectral features. The row-normalized confusion matrix in Figure 4E showed that the model achieved an overall classification accuracy of 86.7% using a balanced test set containing 30 spectra per state. The awake/pre-anesthesia and propofol anesthesia states were classified with high accuracies of 93.3% and 90.0%, respectively. Notably, the recovery state showed a lower classification accuracy of 76.7%, with partial misclassification into awake/pre-anesthesia and anesthesia groups, which due to the recovery state was expected to represent an intermediate physiological and metabolic state rather than a completely independent molecular condition. Finally, the predicted probability assigned to the anesthesia class was extracted as a continuous anesthesia-state probability. As shown in Figure 4F, the propofol anesthesia group showed markedly higher predicted anesthesia probability over 80% than the awake/pre-anesthesia and recovery groups. In contrast, the awake/pre-anesthesia group showed low anesthesia probability, while the recovery group displayed reduced values compared with the anesthesia group, suggesting that breath SERS fingerprints can not only classify anesthesia-related states but also generate a continuous model output reflecting the likelihood of propofol anesthesia-associated breath signatures.

4. Conclusions

In this work, we developed a mesoporous Au foam-based SERS platform for noninvasive breath analysis of propofol metabolites signatures and anesthesia-state discrimination. Firstly, the Au foam chips were fabricated through selective dealloying of Au-Ag alloy films, generating a three-dimensional interconnected ligament-pore architecture with optimized pore size and ligament width of 55 ± 9 nm and 24 ± 4 nm, respectively, exhibiting strong SERS enhancement and high operational robustness with enhancement factor of 6.84×10^5 using 4-MBN as a Raman reporter. The dealloyed Au foam with homogeneous signal distribution (RSD < 9%) and batch-to-batch reproducibility (RSD < 2.5%) showed excellent signal stability output under dry N_2, high-humidity atmospheres, and artificial breath conditions within over 30 days of storage, providing a stable, reproducible, and breath-compatible SERS interface for gas-phase molecular sensing. Then, the molecular fingerprinting capability of the Au foam chip was further validated using propofol and representative propofol metabolites. Distinct SERS fingerprints were obtained for these structurally related molecules. Based on the specific Raman peak assignments, including 1452 cm^{-1} for propofol, 842 cm^{-1} for 4-hydroxypropofol, 1048 cm^{-1} for propofol glucuronide, and 1088 cm^{-1} for propofol sulfate, the PCA analysis of Au foam-derived SERS fingerprints showed clear separation of the four molecules, with PC1, PC2, and PC3 explaining 64.3%, 19.4% and 8.74% of the spectral variance, respectively, which finally achieved an overall accuracy above 85%, supporting reliable molecular recognition of structurally related propofol derivatives. Quantitatively, the SERS responses showed good linearity over 2–75 ppb for all four propofol-realated molecules, with low LODs of 0.847 ppb for propofol, 0.663 ppb for 4-hydroxypropofol, 1.259 ppb for propofol glucuronide, and 1.035 ppb for propofol sulfate. Moreover, taking advantage of the high selectivity of the Raman feature-drived Au foam breath analysis platform, recovery rates above 90% was achieved in spike-recovery experiments at multiple concentration, further confirming the quantitative reliability of the platform in artificial breath matrix. Finally, in clinical application of the discrimination of propofol anesthesia-related states, it was found that the breath SERS score was significantly elevated in the anesthesia state and decreased during recovery, which achieved an overall accuracy of 86.7% for supervised classification, with classification accuracies of 93.3% for awake/pre-anesthesia, reaching an anesthesia-state probability over 80%. The proposed Au foam SERS platform provided a promising noninvasive analytical strategy for perioperative breath analysis, which offerred complementary molecular information related to propofol exposure, metabolism, and recovery, supporting future development of compact optical sensing tools for anesthesia-state assessment.

Supplementary Materials: The following supporting information can be downloaded at: https://media.sciltp.com/articles/others/2606241446285739/MI-26050200-SI.pdf.

Author Contributions: H.Z.: experimental operation, data analysis, and writing (original draft reparation); G.A.: Sample acquirement, data visualization and clinical evaluation; E.F.: project design, writing (reviewing and editing). All authors have read and agreed to the published version of the manuscript.

Funding: National Natural Science Foundation of China (22404125 to E.F.), Tongji University Medicine-X Interdisciplinary Research Initiative (2026-0674-YB-06), Scientific Research Founds of Shanghai Fourth People's Hospital (SY-XKZT-2024-1005 and sykyqd08801 to E.F.), and Shanghai Sailing Program (24YF2733400 to E.F.).

Institutional Review Board Statement: The study was conducted according to the guidelines of the Declaration of Helsinki, approved by the Ethics Committee of Shanghai General Hospital (approval number 2025-192,22 September 2025).

Informed Consent Statement: Informed consent was obtained from all subjects involved in the study. Written informed consent has been obtained from the patients to publish this paper.

Data Availability Statement: All data are available in the article and its Supplementary Information. Additional requests can be directed to the corresponding author.

Conflicts of Interest: The authors declare no conflict of interest.

Use of AI and AI-Assisted Technologies: No AI tools were utilized for this paper.

References

1. Sahinovic, M.M.; Struys, M.M.R.F.; Absalom, A.R. Clinical Pharmacokinetics and Pharmacodynamics of Propofol. *Clin. Pharmacokinet.* **2018**, *57*, 1539–1558.
2. Eleveld, D.J.; Colin, P.; Absalom, A.R.; Stuys, M.M.R.F. Pharmacokinetic-Pharmacodynamic Model for Propofol for Broad Application in Anaesthesia and Sedation. *Br. J. Anaesth.* **2018**, *120*, 942–959.
3. Rosow, C.; Manberg, P.J. Bispectral Index Monitoring. *Anesthesiol. Clin. N. Am.* **2001**, *19*, 947–966.
4. Miekisch, W.; Schubert, J.K.; Noeldge-Schomburg, G.F.E. Diagnostic Potential of Breath Analysis-Focus on Volatile Organic Compounds. *Clin. Chim. Acta.* **2004**, *347*, 25–39.
5. Amann, A.; Miekisch, W.; Schubert, J.; Buszewski, B.; Ligor, T.; Jezierski, T.; Pleil, Risby, J.T. Analysis of Exhaled Breath for Disease Detection. *Annu. Rev. Anal. Chem.* **2014**, *7*, 455–482.
6. Harrison, G.R.; Critchley, A.D.J.; Mayhew, C.A.; Thompson, J.M. Real-Time Breath Monitoring of Propofol and Its Volatile Metabolites during Surgery Using a Novel Mass Spectrometric Technique: A Feasibility Study. *Br. J. Anaesth.* **2003**, *91*, 797–799.
7. Takita, A.; Masui, K.; Kazama, T. On-Line Monitoring of End-Tidal Propofol Concentration in Anesthetized Patients. *Anesthesiology* **2007**, *106*, 659–664.
8. Perl, T.; Carstens, E.; Hirn, A.; Quintel, M.; Vautz, W.; Nolte, J.; Jünger, M. Determination of Serum Propofol Concentrations by Breath Analysis Using Ion Molecule Reaction Mass Spectrometry. *Br. J. Anaesth.* **2009**, *103*, 822–827.
9. Jiang, D.; Li, E.; Zhou, Q.; Wang, X.; Li, H.; Ju, B.; Guo, L.; Liu, D.; Li, H. Online Monitoring of Intraoperative Exhaled Propofol by Acetone-Assisted Negative Photoionization Ion Mobility Spectrometry Coupled with Time-Resolved Purge Introduction. *Anal. Chem.* **2018**, *90*, 5280–5289.
10. Li, X.; Chang, P.; Zhang, W. Online Monitoring of Propofol Concentrations in Exhaled Breath. *Heliyon* **2024**, *10*, e39704.
11. Zeng, J.; Stankovic, N.; Singh, K.D.; Steiner, R.; Frey, U.; Erb, T.; Sinues, P. Breath Analysis of Propofol and Associated Metabolic Signatures: A Pilot Study Using Secondary Electrospray Ionization High-Resolution Mass Spectrometry. *Anesthesiology* **2025**, *143*, 345–356.
12. Meidert, A.S.; Rucz, P.; Angster, J.; Esser, J.; Miklos, A.; Schelling, G. Photoacoustic Detection of Propofol in Breath Gas for Monitoring Depth of Anaesthesia: From Bench to Bedside. *Br. J. Anaesth.* **2025**, *135*, 1203–1211.
13. Fernández-Lodeiro, A.; Constantinou, M.; Panteli, C.; Agapiou, A.; Andreou, C. Breath Analysis via Surface Enhanced Raman Spectroscopy. *ACS Sens.* **2025**, *10*, 602–621.
14. Ding, S.Y.; You, E.M.; Tian, Z.Q.; Moskovits, M. Electromagnetic Theories of Surface-Enhanced Raman Spectroscopy. *Chem. Soc. Rev.* **2017**, *46*, 4042–4076.
15. Pilot, R.; Signorini, R.; Durante, C.; Orian, L.; Bhamidipati, M.; Fabris, L. A Review on Surface-Enhanced Raman Scattering. *Biosensors* **2019**, *9*, 57.
16. Yi, J.; You, E.M.; Hu, R.; Wu, D.Y.; Liu, G.K.; Yang, Z.L.; Zhang, H.; Gu, Y.; Wang, Y.H.; Wang, X.; et al. Surface-Enhanced Raman Spectroscopy: A Half-Century Historical Perspective. *Chem. Soc. Rev.* **2025**, *54*, 3423–3480.
17. Zhou, Y.; Gu, Q.Y.; Qiu, T.Z.; He, X.; Chen, J.Q.; Qi, R.J.; Huang, R.; Zheng, T.T.; Tian, Y. Ultrasensitive Sensing of Volatile Organic Compounds Using a Cu-Doped SnO_2-NiO p-n Heterostructure That Shows Significant Raman Enhancement. *Angew. Chem. Int. Ed.* **2021**, *60*, 26260–26267.
18. Wittstock, G.; Bäumer, M.; Dononelli, W.; Klüner, T.; Lührs, L.; Mahr, C.; Moskaleva, L.V.; Oezaslan, M.; Risse, T.; Rosenauer, A.; et al. Nanoporous Gold: From Structure Evolution to Functional Properties in Catalysis and Electrochemistry. *Chem. Rev.* **2023**, *123*, 6716–6792.
19. Ding, Y.; Kim, Y.J.; Erlebacher, J. Nanoporous Gold Leaf: “Ancient Technology”/Advanced Material. *Adv. Mater.* **2004**, *16*, 1897–1900.
20. Erlebacher, J.; Aziz, M.J.; Karma, A.; Dimitrov, N.; Sieradzki, K. Evolution of Nanoporosity in Dealloying. *Nature* **2001**, *410*, 450–453.
21. Qian, L.H.; Yan, X.Q.; Fujita, T.; Inoue, A.; Chen, M.W. Surface Enhanced Raman Scattering of Nanoporous Gold: Smaller Pore Sizes Stronger Enhancements. *Appl. Phys. Lett.* **2007**, *90*, 153120.
22. Lang, X.Y.; Guan, P.F.; Zhang, L.; Fujita, T.; Chen, M.W. Characteristic Length and Temperature Dependence of Surface Enhanced Raman Scattering of Nanoporous Gold. *J. Phys. Chem. C* **2009**, *113*, 10956–10961.

23. Lang, X.Y.; Chen, L.Y.; Guan, P.F.; Fujita, T.; Chen, M.W. Geometric Effect on Surface Enhanced Raman Scattering of Nanoporous Gold: Improving Raman Scattering by Tailoring Ligament and Nanopore Ratios. *Appl. Phys. Lett.* **2009**, *94*, 213109.
24. Li, F.; Luo, S.; Qu, F.; Wang, D.; Li, C.; Liu, X. Electrochemical Dealloying Preparation and Morphology Evolution of Nanoporous Au with Enhanced SERS Activity. *Coatings* **2023**, *13*, 489.
25. Harmsen, S.; Huang, R.; Wall, M.A.; Karabeber, H.; Samii, J.M.; Spaliviero, M.; White, J.R.; Monette, S.; O'Connor, R.; Pitter, K.L.; et al. Surface-Enhanced Resonance Raman Scattering Nanostars for High-Precision Cancer Imaging. *Sci. Transl. Med.* **2015**, 7, 271ra7.
26. Yamakoshi, H.; Dodo, K.; Okada, M.; Ando, J.; Palonpon, A.; Fujita, K.; Kawata, S.; Sodeoka, M. Imaging of EdU, an Alkyne-Tagged Cell Proliferation Probe, by Raman Microscopy. *J. Am. Chem. Soc.* **2011**, *133*, 6102–6105.
27. Court, M.H.; Duan, S.X.; von Moltke, L.L.; Greenblatt, D.J.; Patten, C.J.; Miners, J.O.; Mackenzie, P.I. Interindividual Variability in Acetaminophen Glucuronidation by Human Liver Microsomes: Identification of Relevant Acetaminophen UDP-Glucuronosyltransferase Isoforms. *J. Pharmacol. Exp. Ther.* **2001**, *299*, 998–1006.
28. Favetta, P.; Degoute, C.S.; Perdrix, J.P.; Dufresne, C.; Boulieu, R.; Guitton, J. Propofol Metabolites in Man Following Propofol Induction and Maintenance. *Br. J. Anaesth.* **2002**, *88*, 653–658.
29. Lussier, F.; Thibault, V.; Charron, B.; Wallace, G.Q.; Masson, J.F. Deep Learning and Artificial Intelligence Methods for Raman and Surface-Enhanced Raman Scattering. *TrAC Trends Anal. Chem.* **2020**, *124*, 115796.
30. Ryzhikova, E.; Kazakov, O.; Halamkova, L.; Celmins, D.; Malone, P.; Molho, E.; Zimmerman, E.A.; Lednev, I.K. Raman Spectroscopy of Blood Serum for Alzheimer's Disease Diagnostics: Specificity Relative to Other Types of Dementia. *J. Biophotonics.* **2015**, *8*, 584–596.